Check for
updates

Advanced testing and characterization of low-temperature cracking in bitumen and mastic

Amir Shabani · **Denis Jelagin** ·
Manfred N. Partl

Abstract Low-temperature cracking is one of the most common failures in asphalt pavements, especially in cold regions. Accordingly, considerable amount of research has been performed in order to understand the low-temperature cracking mechanisms and to propose test methods for characterizing and determining cracking performance of bitumen and asphalt mixtures under freezing conditions. The existing test methods, however, require expensive equipment and skilled technicians; they are thus not well suited for routine tests. As a contribution to mitigate this situation, this study intends to investigate experimentally and characterize numerically the low-temperature cracking behavior of bitumen and mastic materials using a refined thermal cracking test method. The proposed method, the annular restrained cold temperature induced cracking (ARC-TIC) test, allows to determine the low-temperature cracking properties of the mastic and bitumen with a relatively simple setup. In this paper, finite element (FE) modeling is used for evaluating the effect of test parameters on the temperature, stress and strain gradients induced in the specimen during the test. The ARCTIC test is employed to measure cracking temperatures of two bitumen and two mastic materials. The measurements repeatability is examined and the effect of bitumen type on the thermal cracking potential of bitumen and mastic is evaluated. FE modeling is employed to examine the effect of thermomechanical parameters on thermal cracking performance of the materials and to back-calculate fracture stress and strain from measurements. The results highlight the potential of the proposed test and analysis method for evaluation of low-temperature cracking in bitumen and asphalt mastic.

Keywords Mastic · Bitumen · Thermal cracking · Annular restrained cold temperature induced cracking (ARCTIC) test · Viscoelasticity · Finite element method

A. Shabani · D. Jelagin (✉) · M. N. Partl
Department of Civil and Architectural Engineering,
KTH Royal Institute of Technology, Brinellvägen 23,
114 28 Stockholm, Sweden
e-mail: Denis.jelagin@abe.kth.se

A. Shabani
e-mail: Amirsh@kth.se

M. N. Partl
e-mail: Manfred.partl@bluewin.ch

1 Introduction

Thermal cracking is known to be a frequent failure mode in regions affected by diurnal temperature variations. Hence, it received considerable research attention worldwide, both from an experimental and numerical point of view. As a result, the mechanisms and parameters affecting low-temperature cracking resistance are reasonably well understood. As discussed by e.g. Kim et al. [1] the buildup of thermal

stresses and cracks in compacted asphalt mixtures is controlled not only by the magnitude and speed of the thermal loading, but also by their thermal contraction coefficient, viscoelastic properties and tensile strength.

In order to reduce the experimental effort associated with the characterization of low temperature cracking resistance of asphalt mixtures, several attempts have been made to infer their performance from the measurements conducted on the bitumen phase as one of its main components [2]. Generally, the experimental tools for low-temperature testing of bitumen can be grouped into two categories: direct measurement of low-temperature cracking (e.g. with Fraass test) and indirect measurements by correlating low-temperature viscoelastic properties of bitumen with low-temperature cracking performance of mixtures [3]. Among the tests in the second category, Bending Beam Rheometer (BBR) is the most commonly used test method. It has, however, been shown by e.g. Lu et al. [4], and Kommidi and Kim [5] that Dynamic Shear Rheometer (DSR) measurements may be successfully correlated with BBR.

It should be pointed out that the relationship between the low temperature performance of the binder and the compacted asphalt mixture is not necessarily strong. Sebaaly et al. [6] and Wu [7] reported that the low temperature performance of asphalt mixtures corresponds well with BBR and DSR test results, respectively, given that the proper ageing conditions are utilized. At the same time, Zaumanis and Valters [8] observed only a weak relationship between the Fraass breaking point test results and the performance of asphalt mixtures in the Thermal Stress Restrained Specimen Test (TSRST) as well as the Semi-Circular Bending (SCB) test. According to Walubita et al. [9], low temperature rheological properties of bitumen measured with BBR exhibit limited correlation with fracture properties of hot mix asphalt (HMA). The intensity of this correlation was, however, found to vary significantly with the fracture parameters of the materials evaluated in their study. Bueno et al. [10] established the cyclic shear cooling (CSC) failure test as a technique for assessing the low temperature cracking properties of bitumen utilizing DSR equipment. In this fatigue test, the failure progression in bitumen is measured under monotonically reduced temperature resulting in the transition from ductile

to brittle response. As shown by Bueno et al. (2014) the CSC test allows capturing the low temperature damage resistance of a wide range of virgin and polymer modified bitumen with high repeatability. In order to evaluate the resistance of bitumen to failure under a monotonically increasing load, Bueno et al. [11] applied the bitumen fracture toughness test (FTT) according to the European technical specification [12], conducted on beam-shaped specimens with a notch subjected to three-point bending at several different temperatures to infer the bitumen's resistance to low temperature cracking. The bitumen's failure temperature was defined by specifications [12] as the temperature at which the beam deflection at maximum force equals 0.3 mm. Bueno et al. [11] showed that this definition allows to distinguish between low temperature performance of a wide range of modified and unmodified bitumen with a repeatability of less than 2 °C. No attempt has been made however in their study to correlate the measured bitumen performance and the asphalt mixture low temperature cracking.

In the studies summarized above, the resistance of bitumen to thermally induced fracture is inferred from its viscoelastic and/or damage resistance properties at low temperatures, while the effect of the thermal contraction properties of the materials is not considered and measured explicitly. This may be a possible reason for the somewhat weak correlation of bitumen and asphalt mixture test results. Furthermore, the existing test methods are not fully suitable for routine testing in view of the cost of specimen preparation and test equipment involved [13]. In order to address these issues and to establish a practical test for characterizing bitumen resistance to low temperature cracking, Kim [14] developed the Asphalt Binder Cracking Device (ABCD). The ABCD test utilizes the thermal contraction of a ring-shaped bitumen specimen constrained in its center by a hollow Invar core in order to induce thermal stresses in the specimen and relies on strain gauge measurements for determining the fracture initiation point. The ABCD test has been used in several recent studies to characterize a wide range of bitumen [15–18]. In summary, the obtained results indicated that the ABCD measurements have a strong correlation with the AASHTO critical cracking temperature [19]. Furthermore, as noted by Elwardany et al. [20], combining BBR and ABCD data allows better ranking of the bitumen

resistance against pavement surface failures, such as block cracking and raveling than using only BBR results.

In the present study an alternative experimental and analysis methodology to characterize low temperature cracking resistance of bitumen and asphalt mastic materials is proposed, inspired by the research conducted by Kim et al. [21]. The Annular Restrained Cold Temperature Induced Cracking (ARCTIC) test proposed in this study is based on the formation of cracks due to the difference between the contraction coefficient of the ring-shaped specimen and the Invar core in its center. The moment of crack formation is detected based on sound emission analysis from the sound recorded during the test. Accordingly, in contrast to ABCD test, no strain measurements are required and the test is performed on a notch-free specimen. Particular attention is paid to optimize the ARCTIC test parameters, such as specimen geometry and thermal loading, for low temperature damage characterization of mastic materials. As demonstrated by numerous studies, bituminous mastic with large aggregates, i.e. a mixture of bitumen with fine particles smaller than 250 microns, acts as a binding phase in the asphalt mixture, and, accordingly, its influence on the properties of the asphalt mixture is quite profound [22]. At the same time, relatively little attention has been paid to the cracking properties of mastic at low temperatures. This is of particular importance, in context of applying asphalt mixtures with fine gradations, such as microsurfacing and slurry. The present study aims to contribute to addressing this issue by demonstrating how the gap between binder and mastic low-temperature properties may be closed and investigated in more depth than has previously been done.

2 Methodology

In this paper, the proposed ARCTIC test methodology is presented and evaluated experimentally and numerically. The ARCTIC test is employed to measure cracking temperature (T_{cr}) of two bitumen and two mastic materials. The repeatability of the measurements is examined and the effect of bitumen type on the thermal cracking potential of bitumen and mastic is evaluated. The measurements are interpreted in terms of the viscoelastic properties

and thermal contraction coefficients of the tested materials. In order to gain further insight into the test sensitivity to the experimental parameters finite element (FE) modeling is employed. Thermomechanical FE modeling has been used in a number of recent studies to investigate low-temperature performance of bituminous materials, as well as to complement and validate different test set-ups [23–27]. In the present study, the FE modeling of ARCTIC test is performed using measured viscoelastic properties and thermal contraction coefficient of the specimens. Particular attention is paid to temperature, stress, and strain gradients developing in the specimens during testing and correspondingly to their effect on the repeatability of the tests. Based on the modeling results, the effect of the thermomechanical parameters of the material on its thermal cracking performance is evaluated and discussed. Furthermore, feasibility of using FE modeling combined with the DSR viscoelastic characterization to back-calculate fracture stress and strain of the material from the fracture temperature determined in the ARCTIC test is evaluated.

Figure 1 presents the research plan, its steps and the link between the experimental and numerical part of the study. First, a feasibility study is performed to develop a test method for bitumen and mastics eliminating deficiencies of existing restrained ring tests. For this purpose, a prototype of the test setup has been developed which is described in detail in Sect. 4.1. The results of this test are then analyzed to determine T_{cr} of bitumen and mastic and the results are evaluated with respect to their repeatability. The details of this part of study are given in Sect. 4.2. Finally, the results of the tests are also used as input to the FE model to evaluate the effects of test parameters on the temperature, stress, and strain gradients of the specimens and to determine the stress and strain developed in the specimens at T_{cr}. This part is described in detail in Sect. 5.

3 Theoretical background

In this study, bitumen and mastic at low temperatures are described as linear viscoelastic materials and the relations between stress and strain are given by:

Fig. 1 Research Plan
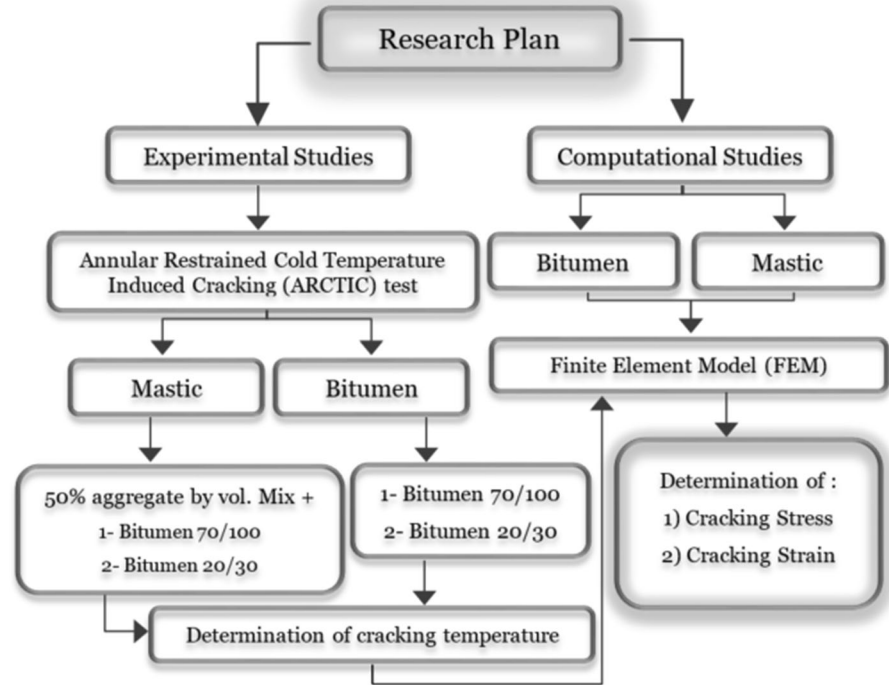
$$S_{ij}(t) = \int_0^t G(t - \tau)\frac{d}{d\tau}e_{ij}(\tau).d\tau \qquad (1)$$

$$\sigma_{kk}(t) = \int_0^t K(t - \tau)\frac{d}{d\tau}\varepsilon_{kk}(\tau).d\tau \qquad (2)$$

where $S_{ij} = \sigma_{ij} - \frac{1}{3}\delta_{ij}\sigma_{kk}$ and $e_{ij} = \varepsilon_{ij} - \frac{1}{3}\delta_{ij}\varepsilon_{kk}$ are the deviatoric stress and strain tensors, σ_{kk} and ε_{kk} are the hydrostatic stresses and strains, and $G(t)$ and $K(t)$ are shear and bulk relaxation moduli respectively. When the ambient temperature drops, the material cools and its internal temperature distribution changes is defined by heat transfer conditions. Generally, the different contributions to the heat transfer are defined by the following equations:

$$q_{\text{Conduction}} = -k.A.\left(\frac{dT}{dx}\right) \qquad (3)$$

$$q_{\text{Convection}} = h.A.\left(T_{\text{S}} - T_{\text{air}}\right) \qquad (4)$$

$$q_{\text{Radiation}} = \varepsilon.\sigma.A\left(T_{\text{S}}^4 - T_{\text{air}}^4\right) \qquad (5)$$

where q is the heat transfer rate (W), T_S is the surface temperature of specimen (K), T_{air} is the temperature of the surrounding media (K), i.e. in this case air temperature in the chamber, k is the thermal conductivity (W $\cdot$m^{-1} $\cdot$K^{-1}), dT/dx is the temperature gradient [K $\cdot$m^{-1}], which is the change in temperature with respect to distance in the direction of heat flow, A is the surface area (m^2), ε is the emissivity of the surface (dimensionless), σ is the Stefan-Boltzmann constant (5.67×10^{-8} W $\cdot$m^{-2} $\cdot$K^{-4}), and h is the convection heat transfer coefficient (W $\cdot$m^{-2} $\cdot$K^{-1}). Equations (3)–(5) show heat transfer by conduction, convection, and radiation, respectively. Radiation heat transfer happens when electromagnetic waves generated by a hot specimen are absorbed by the air. Due to small temperature variations, the insignificant role of this type of heat transmission can be ignored. Therefore, $Q(t)_{\text{Total}}$, which is total amount of heat transferred to/from the specimen over time interval t, is calculated with Eq. (6) and the temperature drop (ΔT) of the specimen can be derived from the energy balance equation (Eq. 7):

$$Q(t)_{\text{Total}} = \int_0^t q_{\text{Conduction}}.dt + \int_0^t q_{\text{Convection}}.dt \qquad (6)$$

$$\Delta T = \frac{-Q_{\text{Total}}}{mc} \qquad (7)$$

where $Q(t)_{\text{Total}}$ is the total heat transferred (J), t is the time (s), m is the mass (kg) and c is the specific heat ($J \cdot kg^{-1} \cdot K^{-1}$) of the specimen. Due to this temperature drop, the material will contract and its thermal strain accumulation is governed by Eq. (8) [28]:

$$\varepsilon_{ii} = \alpha . \Delta T \qquad (8)$$

where ε_{ii} is the thermal strain ($m \cdot m^{-1}$), α is the thermal contraction coefficient (K^{-1}), and ΔT is the temperature change of the specimen (K). In a compacted asphalt mixture, thermal contraction is confined both macroscopically due to the surrounding material and locally due to thermomechanical mismatch between different material phases which cause building up of tensile stresses. When these tensile stresses exceed the materials strength thermal fracture will occur.

4 Experimental study

4.1 ARCTIC test

4.1.1 Specimen preparation

The experimental setup and measurement principles for the present study are shown in Fig. 2. First, a silicone mold with the dimensions given in Fig. 2a was made from liquid silicone with Shore A hardness of 17. An Invar steel cylinder with 100 mm diameter and 50 mm height was used as inner core of the specimen. Invar steel has significantly higher Young's modulus ($E > 200$ GPa) and lower thermal contraction coefficient ($\alpha \approx 1 \times 10^{-6}$/°C) as compared to the tested materials ($E < 5$ GPa and $\alpha \approx 80$–200×10^{-6}/°C), respectively, which is used to induce thermal stresses in the material. When the temperature of specimen drops, the specimen tends to contract as illustrated in Fig. 2b. Since the thermal contraction coefficient of the core is very low compared to the specimen, the core acts as almost perfectly rigid constraint. Thus, tensile stresses in the circumferential direction are induced in the specimen, and fracture occurs when

Fig. 2 Test set-up and measurement principle, **a** Dimensions of the specimen, **b** Strains within the specimen, **c** Schematic view of test set-up, and **d** Prepared specimen within the silicon mold
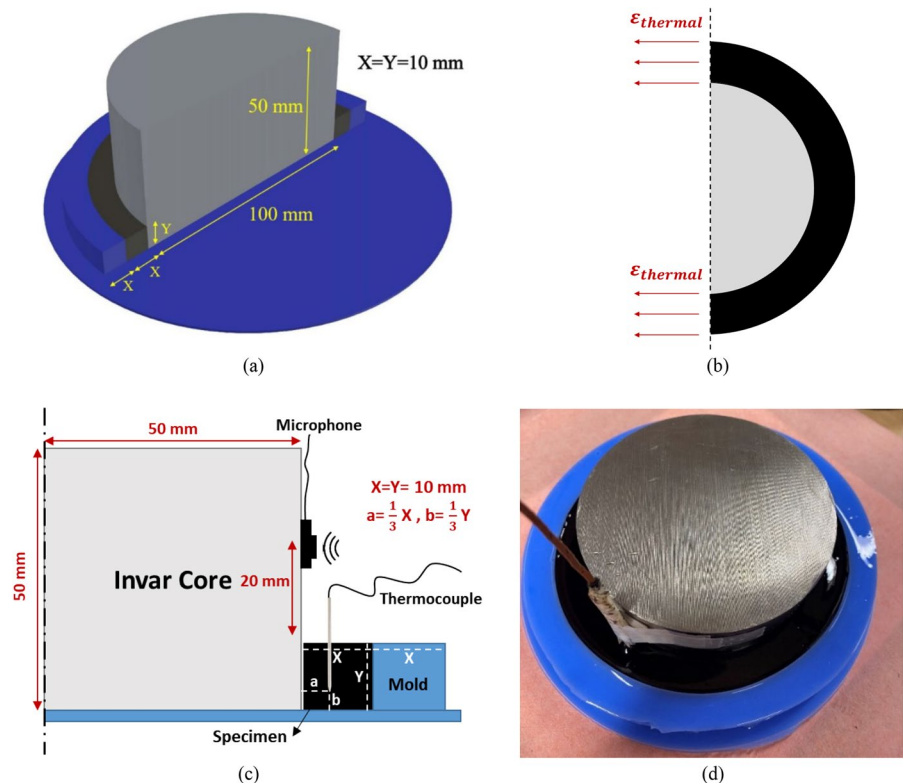
the amount of these stresses exceed the strength of the material. The geometry of the test setup is shown in Fig. 2a. As may be seen, the resulting specimen has a shape of a ring with a square cross-section of 10 mm side length. These specimen dimensions were selected by considering the cooling regime and with the aim of maintaining homogeneity in bitumen and mastics. A brief numerical study using the FE method was also performed to ensure that the selected dimensions of the specimens and the Invar cylinder would result in stresses exceeding the tensile strength of the bitumen and mastic materials during the test. The type K thermocouple wire was placed at the location shown in Fig. 2c to measure the temperature inside the specimen (T_{ab}) during the test. In addition, with the help of a regular 3.5 mm Samsung stereo hands-free microphone attached to the Invar core according to Fig. 2c, the crack sound was recorded for determining the cracking time of the specimen.

In order to prepare the bitumen specimens, the material was first placed in the oven at a temperature of 170 °C for one hour. Then, the liquid bitumen was poured into the silicon mold around the Invar core. In case of mastic specimens, the bitumen and aggregates were heated separately at 170 °C. After the heating, the aggregates were added to bitumen and mixed manually at this temperature until the mixture seemed homogeneous. Then the prepared materials were poured into the mold. After preparation of the specimens, they were conditioned at room temperature overnight to reach ambient temperature. Figure 2d shows a prepared specimen. The ring-shaped silicone mold was removed from the specimen in the last step.

4.1.2 Test procedure

The specimen with the attached microphone at the invar core is placed into a climate chamber at 20 °C and the temperature is reduced to the minimum value of −46 °C at a constant rate of −30 °C/h. After the temperature reaches the minimum value of −46 °C, the specimen is left in the chamber for 2 h to allow the temperature in the specimen to equilibrate. The whole test process takes thus approximately 4 h. The minimum temperature and the cooling rate were chosen from several trial-and-error pre-tests in order to ensure that all bitumen and mastic specimens cracked during the test. In general, a faster cooling rate leads to earlier crack initiation and contributes to a more non-uniform temperature distribution in the specimen. The −30 °C/h rate has been chosen in this study as a reasonable compromise resulting in both reasonable testing times and temperature gradients in the specimen. T_{ab} was recorded during the experiment using a digital thermocouple positioned as illustrated in Fig. 2c. As an example, Fig. 3 shows the applied cooling history of the chamber (T_{CA}) along with the actual air temperature in the chamber (T_{air}) and average T_{ab} of the eight specimens including four bitumens and four mastics with their minimum and maximum variation. As can be seen, the rate of temperature decrease in the sample is not constant and diminishes over time as the difference between T_{ab} and T_{air} decreases. As it is also seen in Fig. 3, the chosen cooling rate results in a reasonably low variability of the temperature between the specimens, with the maximum differences recorded in the order of ± 3 °C

Fig. 3 The applied cooling history (T_{CA}), actual temperature of chamber (T_{air}), and average measured temperature history of mastic and bitumen specimens (T_{ab})
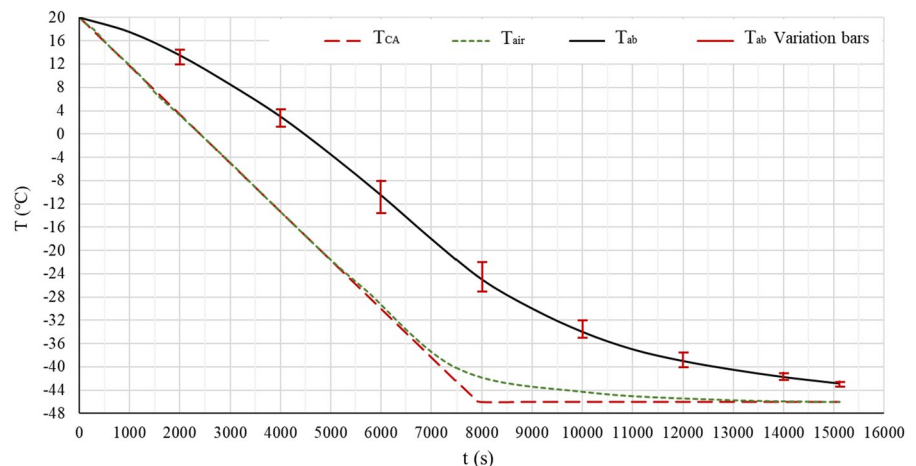
and even lower, within ± 1.5 °C, at the later stage of the test where majority of cracking occurs.

After the test, the specimen is removed from the chamber and the sound recorded during the test is analyzed in order to determine the time of fracture initiation, as detailed below. The fracture initiation time combined with the recorded T_{ab} allows to determine T_{cr}. Audacity digital audio editor software version 1.3 was used for eliminating the background noise of the climate chamber fan. As an example, Fig. 4 shows the recorded sound during the test before and after signal noise reduction for a bitumen specimen. The fracture initiation in the specimen is accompanied by acoustic emission and those emissions may be readily identified from the noise-filtered recording, as seen in Fig. 4b. The multiple peaks seen in Fig. 4b correspond to the initiation of multiple fractures, as discussed in more detail in Sect. 6.1. In the present analysis, the time of first fracture initiation is used to determine T_{cr}.
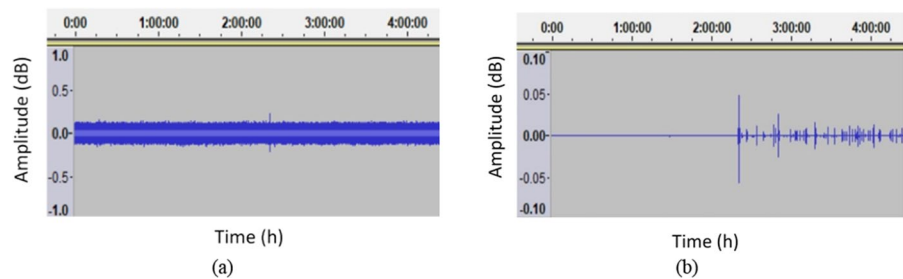
4.2 Materials

Four ARCTIC tests were performed for two bitumen and two mastic materials. The two bitumens used in this research were 20/30 and 70/100 penetration grade with the properties according to EN 12591 [29]. Mastics with 50% aggregate content and the same binder content were prepared using natural crushed granite aggregates with a maximum aggregate size of 0.25 mm. In what follows, the four tested materials are referred to by their binder penetration grade and the material type, i.e. "mastic 20/30" refers to the mastic prepared with 20/30 grade bitumen. The temperature distribution in the specimen during cooling is controlled, in addition to it's geometry and thermal load, by the material's specific heat capacity, c [J $\cdot$kg^{-1} $\cdot$K^{-1}], thermal conductivity, k [W $\cdot$m^{-1} $\cdot$K^{-1}], and boundary convection heat transfer coefficient, h [W $\cdot$m^{-2} $\cdot$K^{-1}]. The amount of thermally induced deformation in specimen is in turn controlled by the thermal contraction coefficient α [K^{-1}], and the magnitude of the accumulated stress is dependent on the viscoelastic properties of the material, expressed e.g. through its dynamic modulus, E [N $\cdot$m^{-2}]. The thermal and mechanical properties of the materials used in the analysis of experimental results and in FE modeling are summarized below.

4.2.1 Thermal properties

The thermal properties of the materials are listed in Table 1. The thermal contraction coefficients (α) for the four materials were measured as follows. First, a cylindrical silicone mold with a diameter of 10 mm and a height of 100 mm and cut along its height, for

Fig. 4 Recorded sound emission **a** before, and **b** after noise cancellation for Bitumen 70/100 specimen

Table 1 Characteristic properties of materials used

Property	Material		
	Bitumen 70/100 & 20/30	Mastic 70/100 & 20/30	Invar
Contraction coefficient (α) (K^{-1})(10^{-6})	152	69.2	1.3
Heat transfer coefficient (h) (W $\cdot$m^{-2} $\cdot$K^{-1})	20	20	20
Specific heat (c) (@ 20 °C) (J $\cdot$kg^{-1} $\cdot$K^{-1})	1800 [31]	1000 [31]	515
Density (D) (kg $\cdot$m^{-3})	1000 [32]	2000 [33]	8110
Conductivity (k) (W $\cdot$m^{-1} $\cdot$K^{-1})	0.17 [34]	0.83 [35]	10

easy demolding, was prepared. During sample preparation, adhesive tape is used to hold the cut together. The materials were heated up to 160 °C and carefully poured into the mold. After pouring, (Fig. 5a), the specimens were kept at 7 °C for 4 h to harden. Then the specimens demolded and their initial length was measured at 7 °C as initial temperature according to Fig. 5b. The specimens were then placed on a silicone plate into a climate chamber and conditioned at −18 °C for 4 h and their length was measured again. Their contraction coefficient (α) was calculated than from:

$$\alpha = \left(\frac{1}{L_0}\right).\left(\frac{\Delta L}{\Delta T}\right) \qquad (9)$$

where L_0 is the initial length of the specimen (m) and ΔL is the change in the length of the specimen (m) due to temperature changes ΔT (K or °C).

The heat transfer coefficient (h), is needed to define the convection boundary conditions on the free surfaces of the specimen, cf. Equation (4). For the case of forced convection h is defined by the following equation [30]:

$$h = 12.12 - 1.16V + 11.6V^{1/2} \qquad (10)$$

where V is the relative speed between the specimen and the air inside the chamber (m/s). From the FE simulations of the test, it has been found that $V = 0.57$ m/s is a reasonable estimation to predict the temperature measured by the thermocouple by simulated model at the same location.

Other properties of bitumen and mastic, such as density, conductivity, and specific heat, listed in
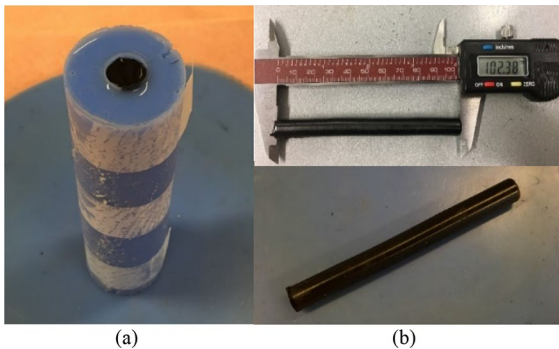
Fig. 5 a Prepared specimen in the mold, and **b** Demolded specimen

Table 1, were determined based on the literature review. The references used for each of these properties are also provided in Table 1. It is assumed that penetration grade of the bitumen does not affect the specimen's thermal properties significantly. Hence, in the Table 1 the same properties are presented for 70/100 and 20/30 materials. The properties of the Invar material were also in accordance with the measurements and information provided by its manufacturer e.g. Special Metals Co.

4.2.2 Viscoelastic properties

The magnitude of stresses induced in the specimens is controlled by their viscoelastic properties, including complex dynamic modulus (G^*), storage modulus (G'), and loss modulus (G''). These parameters were measured using the DSR at $T = −10, 0, 10, 20,$ and 30 °C in the angular frequency range of $\omega = 0.1$–62 rad/s and at a maximum shear strain ($\gamma_{\max}$) of less than 2.3% for bitumen and mastic 70/100. The attention is focused on the 70/100 materials because of their widespread application in Swedish weather conditions. The DSR measurements were used to construct the master curve at $T_r = 0$ °C with the shift factors determined using the Williams–Landel–Ferry (WLF) equation:

$$\log(a_T) = \frac{-C_1(T - T_r)}{C_2 + (T - T_r)} \qquad (11)$$

where $\log(a_T)$ is the logarithm of the shift factor, T is the actual temperature (°C), T_r is the reference temperature for constructing the master curve and C_1 and C_2 are constants. Once C_1 and C_2 in the WLF equation are determined, a_T values for temperatures down to −40 °C are extrapolated from measurements. The following sigmoidal function is fitted to the master curve.

$$G^* = a + \frac{b}{1 + e^{c + d\omega}} \qquad (12)$$

where G^* is the complex modulus (Pa), ω is angular frequency (rad/s) and a, b, c and d are constants. The determined shift factors and the master curves at $T_r = 0$ °C are shown in Fig. 6a and b respectively. For the FE modeling, Poisson's coefficient is assumed to be 0.35 and constant with temperature and measured
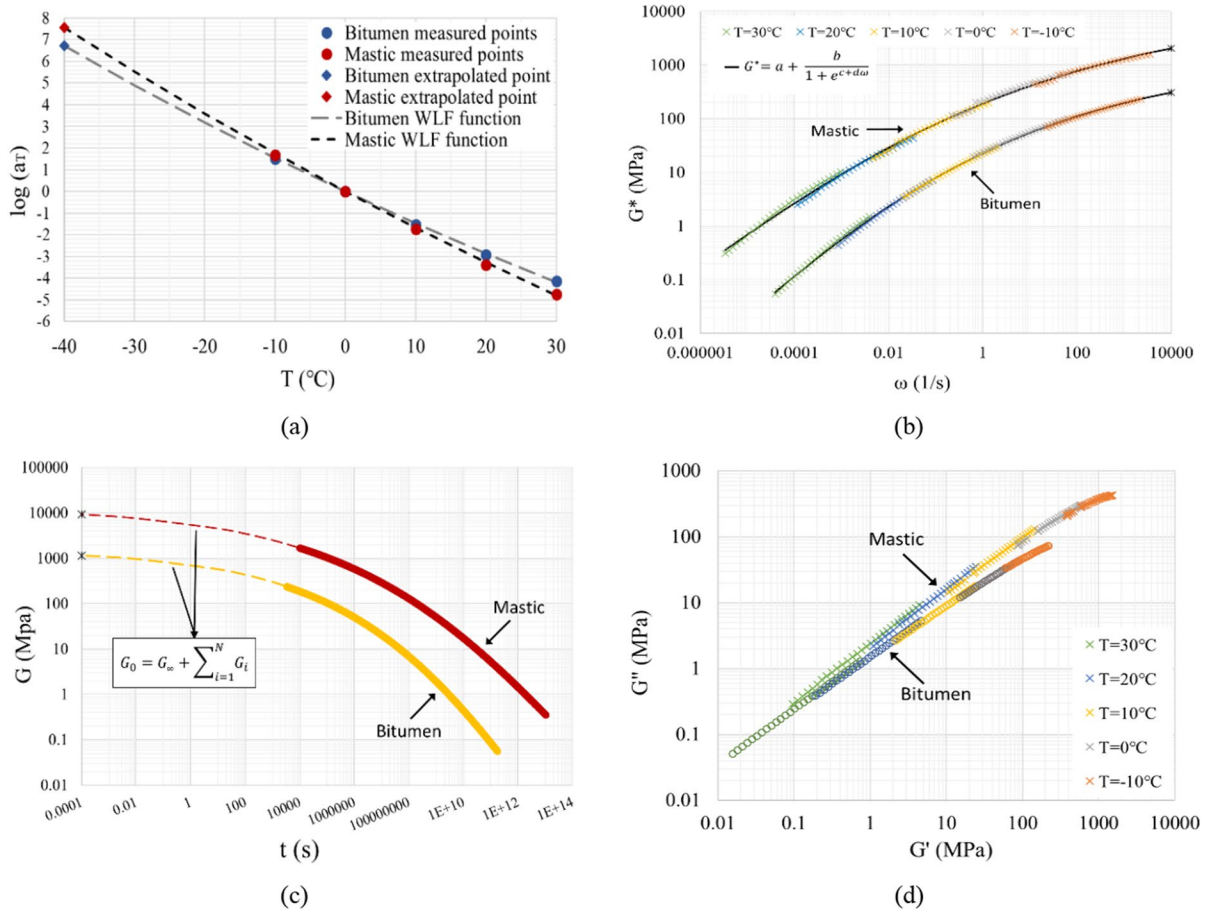
Fig. 6 Viscoelastic properties of bitumen and mastic 70/100 **a** WLF diagram and shift factors, **b** Master curve at $T_r = 0$ °C, c Relaxation modulus at $T_r = -40$ °C, **d** Cole–Cole diagram

$G^*(\omega)$ is converted to the relaxation modulus, $G(t)$, by using generalized Maxwell model according to:

$$G_{(t)} = G_0 - \sum_{i=1}^{N} G_i \left[1 - e^{-t/\tau_i} \right] \qquad (13)$$

where G_0 is the instantaneous shear modulus, N is the number of elements in the Prony series, and Gi and τi are the modulus and relaxation time, respectively, for the ith element of the Prony series. The Prony series itself is obtained by optimizing the following equations based on Park and Schapery [36] for thirteen points:

$$G\prime_{(\omega)} = G_\infty + \sum_{i=1}^{N} \frac{\omega^2 \tau_i^2 G_i}{\omega^2 \tau_i^2 + 1} \qquad (14)$$

$$G_\infty = G_0 - \sum_{i=1}^{N} G_i \qquad (15)$$

where G_∞ is the long-term modulus once the material is totally relaxed. Table 2 shows the obtained Prony series parameters. The resulting $G(t)$ is shown in Fig. 6c at $T_r = -40$ °C where dashed parts of the curves indicate the extrapolated regions. As may be seen from Fig. 6c a considerable amount of extrapolation is involved when estimating specimen's viscoelastic properties at low temperatures. This, of course, introduces a certain degree of uncertainty into the FE modeling. In future studies, it will be evaluated, whether a viscoelastic characterization at lower temperatures will improve the modeling accuracy. Based on the results presented in Fig. 6c, the mastic is approximately 9 times stiffer as compared

Table 2 Obtained Prony series parameters

Bitumen		Mastic	
g_i/k_i	τ_i	g_i/k_i	τ_i
0.2920	2.16E+03	0.3071	8.939E+03
0.2115	9.74E+03	0.2197	5.136E+04
0.1707	4.38E+04	0.1711	2.951E+05
0.1249	1.97E+05	0.1209	1.696E+06
0.0857	8.89E+05	0.0801	9.743E+06
0.0539	4.00E+06	0.0487	5.598E+07
0.0312	1.80E+07	0.0273	3.216E+08
0.0164	8.11E+07	0.0140	1.848E+09
0.0079	3.65E+08	0.0066	1.062E+10
0.0034	1.64E+09	0.0028	6.101E+10
0.0013	7.40E+09	0.0011	3.506E+11
0.0005	3.33E+10	0.0004	2.014E+12
0.0002	1.50E+11	0.0002	1.157E+13

to bitumen and, accordingly, at the same level of thermal contraction, it may be expected to accumulate more stresses. At the same time, as reported in Table 1, its thermal contraction coefficient is approximately 2.2 times lower as compared to bitumen which would reduce the amount of material contraction. The interplay between these two competing effects will be evaluated numerically in Sect. 6.2.

5 Computational studies

FE modeling was used in this study to evaluate geometry effects of the experimental setup and the cooling history on the distribution of temperature and thermally induced stresses in the specimen. Furthermore, the model was also used to back-calculate the tensile stresses and strains of the specimens at time of fracture from T_{cr}. A 2D axisymmetric model of the ARCTIC test was developed using Abaqus 2017 software. The model is used to simulate the tests performed on the bitumen and mastic 70/100 specimens.

The ARCTIC test was modeled in two steps. First, a heat transfer model was used to evaluate the temperature distribution in the specimen as the temperature decreases, taking into account the convective boundary conditions at the free surface of the specimen. In a second step a thermomechanical model was used to evaluate the effect of the obtained temperature distribution on the specimen's thermal contraction and the induced thermal stresses and strains.

As an outcome of the heat transfer model, the temperature distribution in the specimen was determined and the obtained temperature at the free surface of the specimen (T_S) was used as a boundary condition in the thermomechanical model. The model's geometry and mesh is presented in Fig. 7 along with the location of the thermocouple. Based on a numerical sensitivity assessment, the coupled temperature-displacement element type with mesh sizes of 0.002 and 0.0002 m was selected for the Invar core and bitumen/mastic specimen, respectively.

The boundary conditions indicated in Fig. 7c for the two models were as follows. In the heat transfer model a tie constraint was imposed along the boundary between the specimen and the core (line A), postulating that $T_I = T_S$ at the adjacent material points.
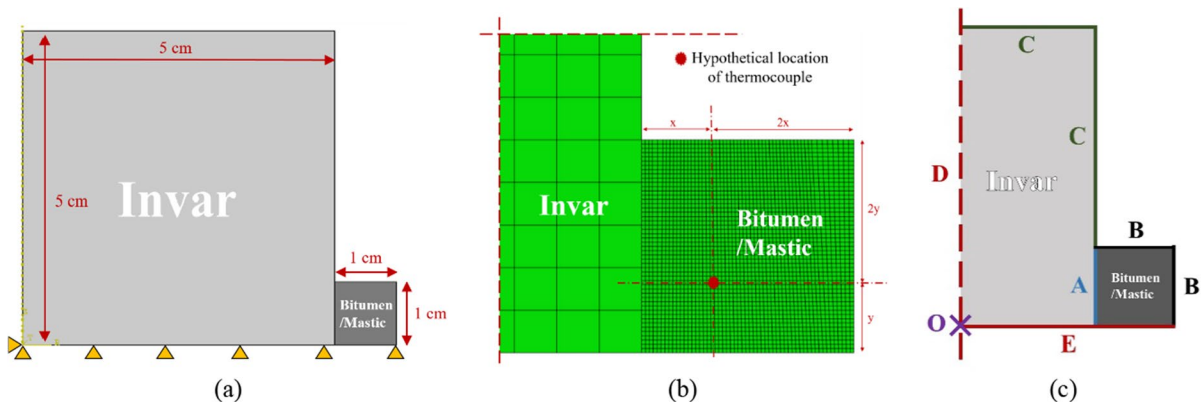
Fig. 7 **a** Geometry, **b** Mesh grid, and **c** Boundary conditions of the proposed model

Where T_I is the temperature at the surface of the invar core and T_S is the temperature at the specimen surface. Along the free surface of the specimen and Invar core (lines B&C) the convection boundary condition was imposed according to T_{air} in Fig. 3. Since there was no direct connection with the air along the axis of rotational symmetry and the bottom boundary of the specimen (lines D&E), the heat flux was assumed to be zero and no boundary condition was defined here in both models.

In the thermomechanical model, the mechanical interaction between specimen and Invar core (line A) was defined through the contact boundary condition. Lagrangian friction formulation was used with a friction coefficient of 0.7. Although there was no single value for the friction coefficient and it usually varies between 0.3 and 0.7 depending on a number of factors, this value was chosen based on the literature review to take into account the maximum influence of friction on the result [37]. Temperature history at the boundary (lines B&C) obtained from the heat transfer model was used as temperature boundary condition along the same boundary in the thermomechanical modeling. At the point O and at the bottom boundary (line E) the horizontal and vertical displacements were set to zero respectively. The viscoelastic properties of bitumen and mastic for the thermomechanical model were set based on the DSR measurements presented in Fig. 6 and Table 2 and the thermal properties of the materials were set following Table 1.

In Fig. 8, temperature histories at the location of the thermocouple are presented as calculated by the

heat transfer model for the bitumen (T_{BM}) and mastic (T_{MM}) specimens. For comparison, the average T_{ab} for the bitumen and mastic specimens 70/100 is also shown, along with T_{CA} and T_{air}. It can be seen that T_{BM}, T_{MM}, and T_{ab} are very close to each other with the deviations staying within the experimental scatter throughout the test. This confirms that the thermal load is captured accurately in the simulations. The temperature history obtained at the thermocouple location with the thermomechanical model is basically identical with the one presented in Fig. 8 and it is omitted here for briefness.

The accuracy of stress analysis was validated by comparing the stress distributions obtained with the thermomechanical model with the analytical solution for the thick-walled elastic pipes. In a cylindrical coordinate system this solution is expressed as follows [38]:
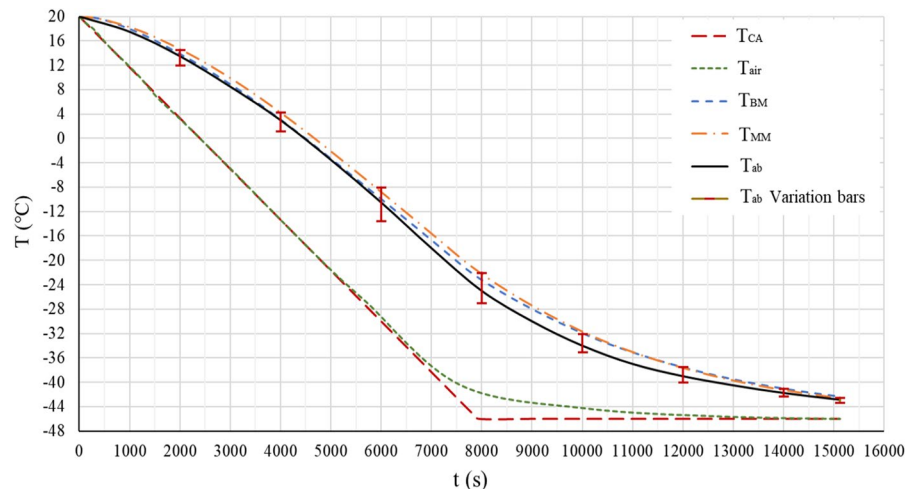
$$\sigma_r = \frac{pa^2}{b^2 - a^2}\left(1 - \frac{b^2}{r^2}\right) = p \cdot \frac{k^2}{1 - k^2}\left(1 - \frac{b^2}{r^2}\right) \quad (16a)$$

$$\sigma_\theta = \frac{pa^2}{b^2 - a^2}\left(1 + \frac{b^2}{r^2}\right) = p \cdot \frac{k^2}{1 - k^2}\left(1 + \frac{b^2}{r^2}\right) \quad (16b)$$

$$\sigma_z = p \cdot \frac{k^2}{1 - k^2} \quad (16c)$$

where p is internal pressure of pipe (MPa), $k = d/D = 2a/2b$, a and b are internal and external

Fig. 8 Calculated temperature history of the heat transfer model compared to the measured temperatures

radius of pipe (mm) respectively, and r is the radius to the desired point ($a < r < b$).

In order to perform the comparison, the thermo-mechanical model was used with the elastic specimen assumption with its shear modulus, G set to G_∞, cf. Table 2. The pressure distribution along the boundary between the specimen and the Invar core was extracted and used as an input to Eqs. (16a–c). The calculated σ_r and σ_θ were compared with the obtained σ_{11} and σ_{33} along the line B in the model. The maximum deviation between analytical and FE results was found to be below 10% for both bitumen and mastic specimens, indicating that the model captures the stress distribution in the specimen well.

6 Results

In this section, first, the experimental results concerning ARCTIC test measurements are presented and discussed. Then the results of the modeling and numerical analysis are given.

6.1 Experimental results

In Fig. 9 an example of the acoustic emission measured for each of the materials tested is shown as a function of time. The measurements in Fig. 9 are presented after the noise removal procedure presented in Sect. 4.1.2. Obviously, several emission events occur in the bitumen specimens, while only one event occurs in the mastic. As also shown in Fig. 9c and d, the amplitude of the sound emission in the mastic is more than four times larger than the amplitudes observed for the bitumen specimens (Fig. 9a and b). These events, which represent a change in the amplitude of the recorded sound, are attributed to crack formation in the specimen and can thus be used to identify the time of cracking during the test, as discussed in Sect. 4.1.2. The acoustic emission patterns in Fig. 9 indicate that fracture induced in bitumen and mastic materials differs qualitatively. Namely, a large number of smaller cracks are formed in bitumen specimens, while in mastic specimens a single main crack is formed.

Typical fracture patterns in bitumen and mastic specimens are depicted in Fig. 10. Obviously, the type of specimen affects the type and quantity of cracks. While the majority of the cracks are oriented perpendicular to the Invar core, following the fracture mechanism illustrated in Fig. 2b, some secondary cracks appear also in the circumferential direction, which may be attributed to stress concentrations arising from gluing the specimen to the core. In bitumen 70/100 specimens, a large number of cracks is formed, and only some of them go through full depth of the specimen, while in bitumen 20/30 specimens fewer cracks are created and most of the cracks propagated through the depth of the specimen. In case of mastic specimens, only one single crack occurred in the majority of the tests on both 70/100 and 20/30 materials. In some cases,

Fig. 9 Acoustic emission measured for **a** Bitumen 20/30, **b** Bitumen 70/100, **c** Mastic 20/30, and **d** Mastic 70/100
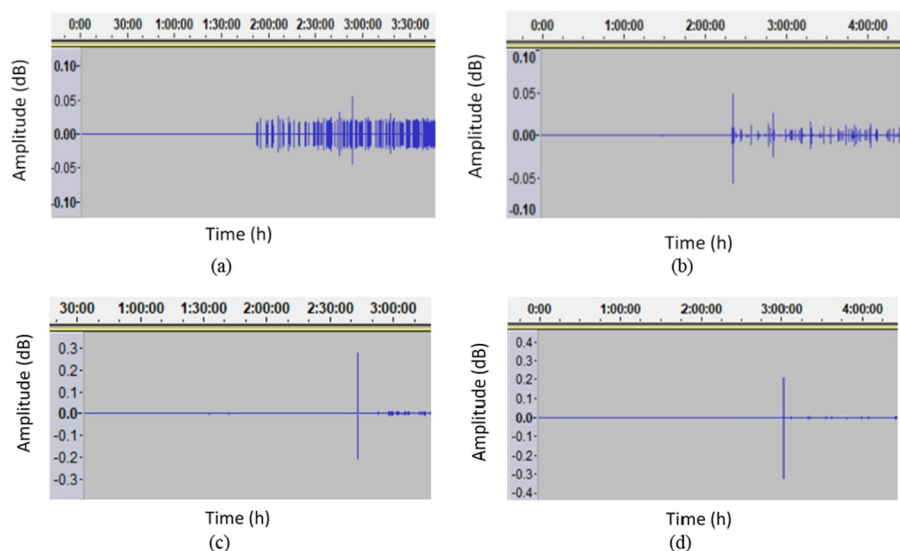
Fig. 10 The fracture pattern in different materials **a** Bitumen 70/100 **b** Bitumen 20/30 **c** Mastic 70/100 **d** Mastic 20/30


(a)　　　　　　*(b)*

(c)　　　　　　(d)
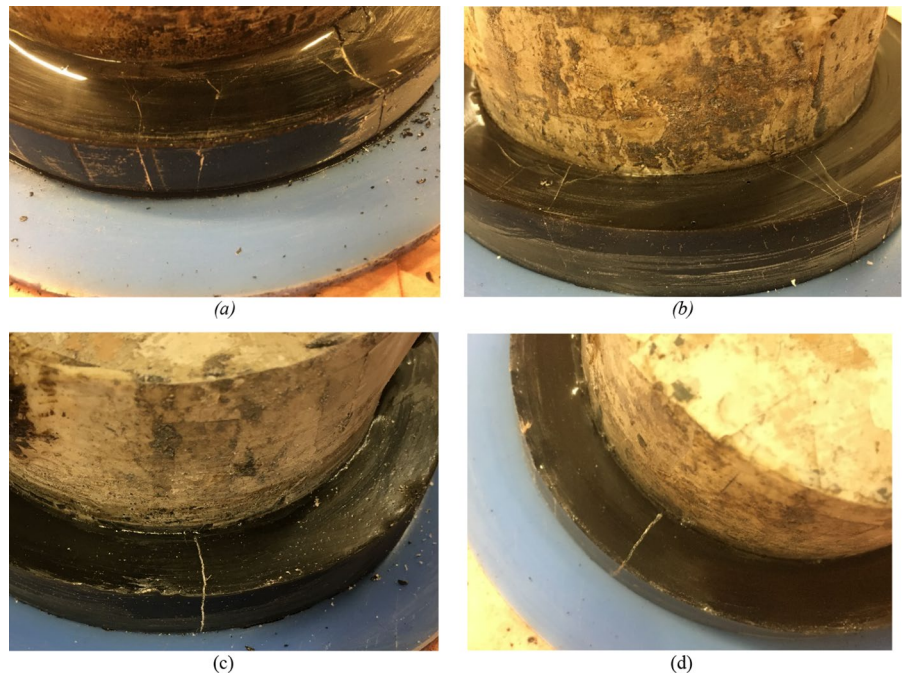
additional cracks appeared, but the total number of cracks in mastics never exceed three, which is significantly less than in the bitumen tests. The observations illustrated in Fig. 10 are thus qualitatively in line with the acoustic emission patterns illustrated in Fig. 9. It should also be pointed out that in some cases, cracks were observed passing through the point where the thermocouple was inserted. Thus, some effects on the measurements from stress concentrations at the thermocouple location cannot be excluded. However, cracks passing through the thermocouple point were observed in less than 50% of

cases. Accordingly, this effect is not expected to be the dominating one.

As discussed in Sect. 4.1.2, T_{cr} for each specimen are identified as specimen temperatures at the moment of first acoustic emissions. In Fig. 11 the measured T_{cr} values are presented for all the materials examined. In order to give a certain insight into the scatter of the measurements, the individually measured T_{cr} values of all specimens are shown along with the mean value of four measurements for each material. As may be seen, T_{cr} is significantly lower in the bitumen and mastic 70/100 as compared to

Fig. 11 Cracking Temperature (T_{cr}) of specimens
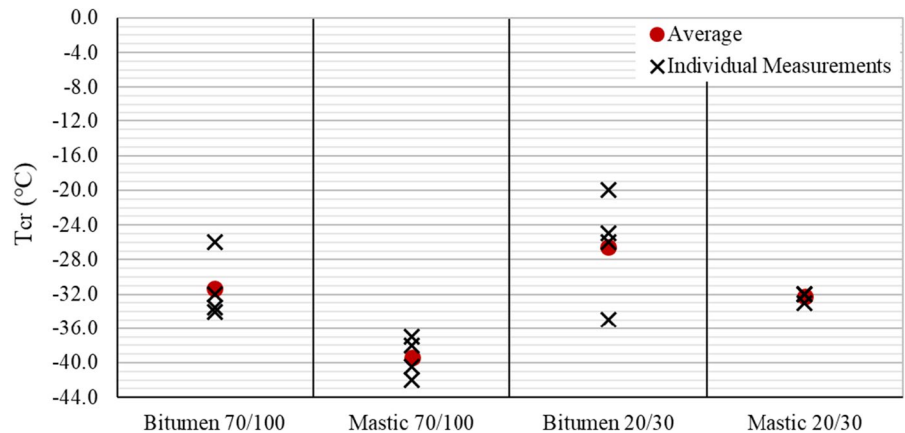
the 20/30 materials, which is somewhat expected as 70/100 materials are more compliant and thus accumulate less thermal stress at the same amount of thermal contraction. Furthermore, both 20/30 and 70/100 mastics show much better low temperature cracking performances as compared to the corresponding bitumens. The measurements on mastic also have significantly lower scatter as compared to bitumen. The higher resistance of mastic to thermal cracking may be partially explained by its lower thermal contraction coefficient, as presented in Table 1. The presence of aggregates in mastic may also increase its tensile strength, as the rigid inclusions put constraints on the crack propagation path. The lower scatter in mastic measurements, is attributed to the higher amplitude in acoustic signals than in bitumen, as illustrated in Fig. 9. Hence, lower amplitude signals, as seen in case of bitumen may, in some cases, be over-shadowed by the noise, which contributes to the measurement uncertainty.

6.2 Computational results

In order to examine the influence of test parameters on measurements repeatability, the temperature and stress distributions induced in the specimen during the ARCTIC test are examined numerically for bitumen and mastic 70/100. In Fig. 12 temperature distribution and the maximum principal stress are presented for the time when T_{BM} and T_{MM} corresponds to the average T_{cr} given in Fig. 11. The deformed shape of the specimens is scaled by a factor of 50, in order to better visualize the induced deformations. As temperature and stress magnitudes induced in bitumen and mastic specimens differ significantly, different color scales are used for the contour plots. As seen in Fig. 13a and b, the bitumen specimen deforms considerably more as compared to the mastic one. There is also a noticeable constraint against the vertical deformation of the specimen from the Invar core, which may be expected to contribute to shear cracking at the specimen to core boundary. There is also a considerable temperature gradient through both mastic and bitumen specimens, with the outer surface of the specimens being significantly colder as compared to the boundary between the specimen and the Invar core. This thermal gradient introduces a certain uncertainty into the determination of T_{cr},

as the location of the first crack does not necessarily correspond to the location of the thermocouple. This uncertainty, as well as the influence of the cooling rate, is explored in more detail below. As seen in Fig. 12c and d, the maximum principal stress induced in the specimen is higher at the boundary between the specimen and Invar core. This stress accumulation, together with other parameters including limited horizontal and vertical movement and a lack of relaxation ability, makes this area important for fracture formation. The maximum principal stress is furthermore oriented in the circumferential direction. Accordingly, the majority of cracks is expected to start at the specimen/core boundary and propagate in the radial direction, which is in qualitative agreement with the observations illustrated in Fig. 10. The maximum principal strain distribution is qualitatively similar to the presented principal stress and is omitted here for briefness.

In order to evaluate quantitatively the effect of the cooling rate on the temperature gradient and thus on the uncertainty associated with the determination of T_{cr}, the temperature amplitudes within the specimen are presented in Fig. 13a and b as a function of T_{ab}. Temperature amplitudes, T_A, presented in Fig. 13 are defined as:

$$T_A = T_{max} - T_{min} \tag{17}$$

where T_A is the temperature amplitude, and T_{max} and T_{min} are the maximum and minimum temperatures within the specimen. The T_A in Fig. 13a are presented as obtained from simulations of the ARCTIC test with a cooling rate of 30 °C/h (i.e. as used experimentally). For reference purposes, the temperature interval where cracking was initiated is also shown in Fig. 13a as a grey shaded area. As shown in Fig. 13a, the temperature gradients in both bitumen and mastic 70/100 specimens are quite significant and reach a maximum of approximately 18 and 7 °C for bitumen and mastic specimens respectively. Lower gradients in mastic specimens are explained by their higher thermal conductivity of mastic as compared to bitumen, cf. Table 1. At the same time, the temperature gradients reach their maximum at $T_{ab} = -18$ °C and the temperature in specimens starts to become more uniform after that point. As a result, the maximum T_A at the temperatures when cracking starts is somewhat
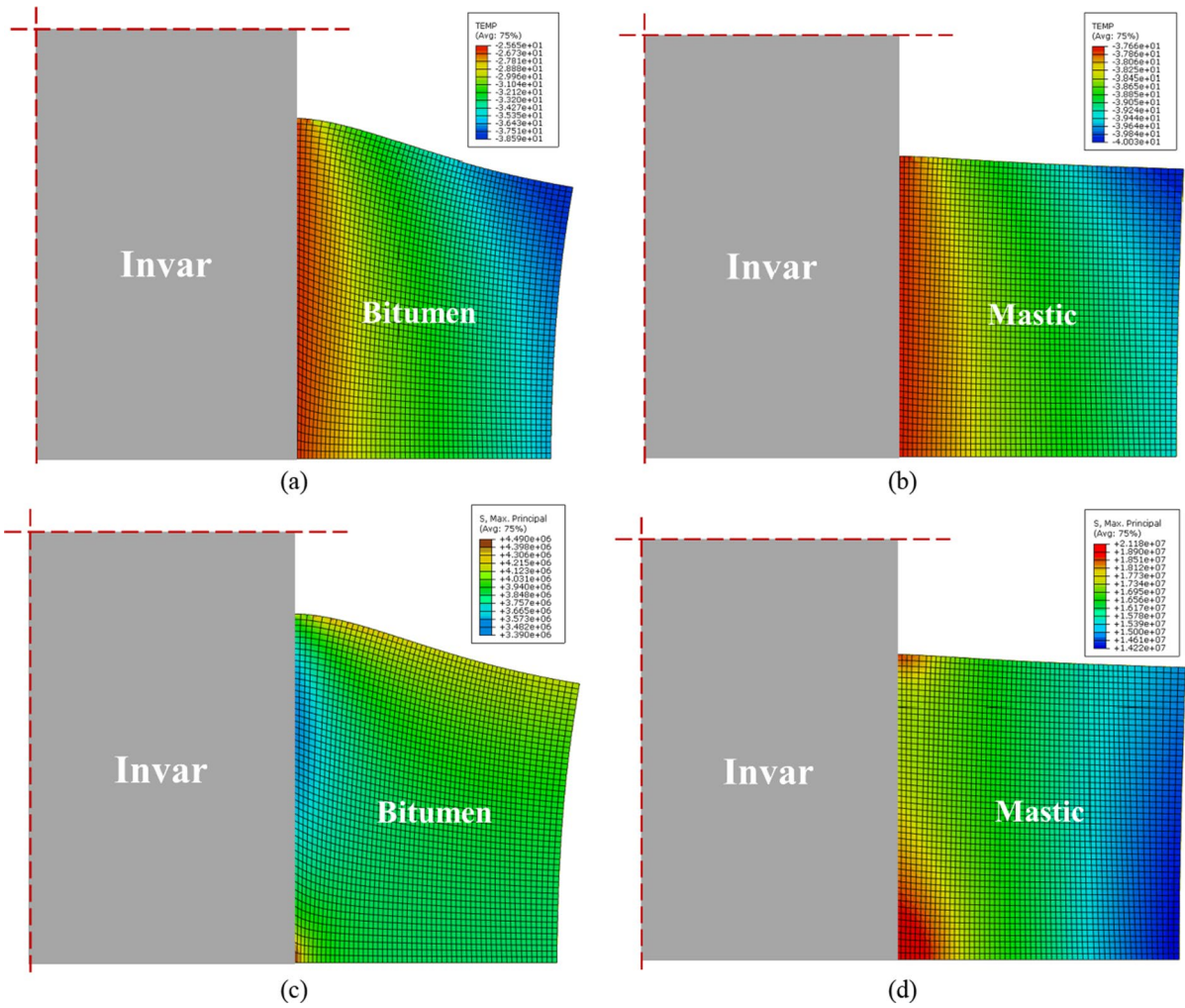
Fig. 12 **a** Temperature distribution of bitumen 70/100, **b** Temperature distribution of the mastic 70/100, **c** Maximum principal stress of bitumen 70/100, and **d** Maximum principal stress of mastic 70/100 at the average T_{cr}
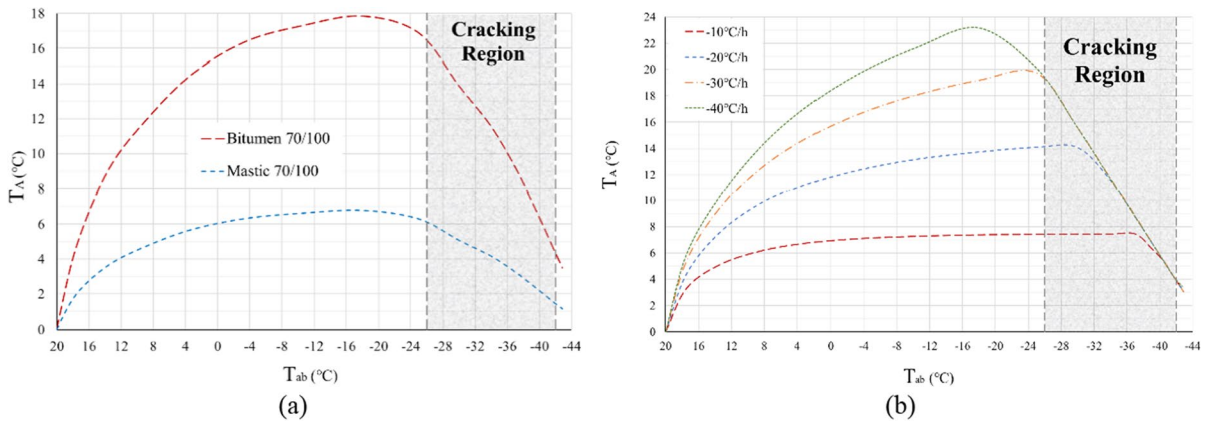

Fig. 13 T_A of **a** bitumen and mastic 70/100 at cooling rate -30 °C/h, and b bitumen 70/100 at different cooling history

lower, i.e. below 16 and 7 °C for bitumen and mastic respectively.

In order to explore the effect of cooling rate, the T_A calculated for the ARCTIC test on bitumen 70/100 specimens are presented in Fig. 13b for the cooling rates of -10, -20, -30 and -40 °C/h. The results for mastic specimens are qualitatively similar and omitted for briefness. Obviously, temperature uniformity at cooling rates of -10 and -20 °C/h is higher than at -30 °C/h. However, temperature uniformity alone may not be sufficient to determine the optimum cooling rate for the test. It is important to consider other factors, such as maximum tensile stress during testing.

At the same time, the lower cooling rate will increase the amount of relaxation in the specimen and accordingly decrease the tensile stresses in the material. This effect is explored quantitatively in Fig. 14, where the average of maximum principal stress for
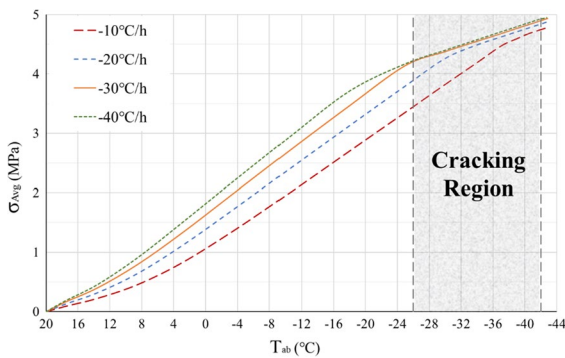
Fig. 14 σ_A versus T_{ab} in Bitumen 70/100 at different loading rate

bitumen 70/100 (σ_A) is presented as a function of T_{ab}, for the same cases as in Fig. 13b. The figure shows that with increasing cooling rate the maximum tensile stress increases at the same T_{ab}. Accordingly, the optimal cooling rate of the test should be chosen by balancing the need for a temperature distributions as homogeneous as possible with the need to induce the tensile stresses exceeding the strength of the material. The cooling rate of -30 °C/h used in this study, allows to induce fracture in all the specimens while keeping the gradients in the specimens within a reasonable range. More in depth evaluation is, however, needed for a larger range of materials.

In order to identify stresses and strains at failure from the ARCTIC test measurements, the maximum principal stresses and strains along the inner vertical boundary of the specimen are averaged at the moment when T_{ab} reaches T_{cr} according to Fig. 11. The stresses and strains at failure for bitumen and mastic 70/100 are presented in Fig. 15 as obtained from the individual measured T_{cr} as well as mean T_{cr}. As seen in Fig. 15a the average stress at failure (σ_{Avg}) for the mastic 70/100 is approximately 4.5 times higher as the ones calculated for the bitumen 70/100 specimens. This result is also comparable to that of Rochlani et al. [39], who evaluated the performance of mastic at low temperatures using the Dresden cryogenic (DDC) test. They also found that the final cryogenic stresses exerted in mastic was 2–4 times higher as compared to the base bitumen. This may be explained by the fact that aggregates in mastic serve as crack propagation inhibitors thus increasing the tensile strength of the material. The higher stiffness of mastic is also another important factor here [40].
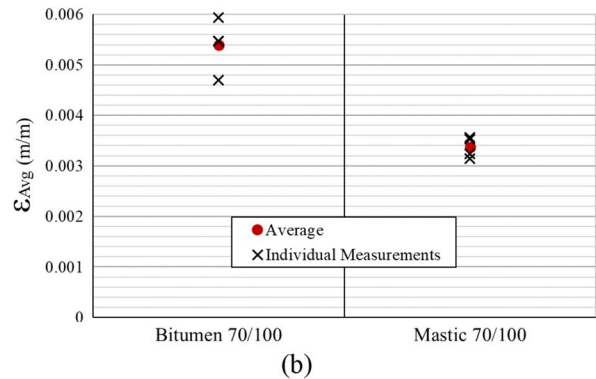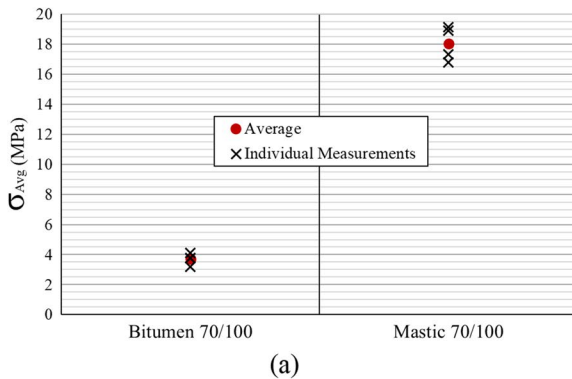
Fig. 15 Average maximum principal **a** stress, and **b** strain at T_{cr} at the contact surface of core and specimen

The strains at failure (ε_{Avg}), presented in Fig. 15b, display an opposite trend, with bitumen accumulating significantly more strains as compared to mastic, which is expected as the thermal contraction coefficient of mastic is about half that of the bitumen, as shown in Table 1. The results presented in Figs. 11 and 15 indicate that the addition of fine aggregates alters the material resistance to thermal damage profoundly, both with respect to T_{cr} and with respect to stresses and strains induced within the material. This highlights the importance of considering mastic properties when optimizing asphalt mixtures for low temperature performance.

7 Conclusions

In this study, a low temperature cracking test method named Annular Restrained Cold Temperature Induced Cracking-Test (ARCTIC-test) is proposed and evaluated experimentally and numerically. In the experimental part, the temperature responses of bitumen and mastic specimens during cooling are measured and the cracking temperature of the specimens is determined by analyzing acoustic emission signals from the specimen during the test. In the modeling part, the stresses and strains of the specimens are calculated using thermomechanical FE modeling and by considering the experimentally determined cracking time. The FE modeling has also been employed to evaluate the effects of the cooling rate as well as temperature gradient and tensile stress magnitude induced during the test. The main outcomes of the present study can be summarized as follows:

- The type of specimen affects the type and quantity of cracks and the shape of the fracture which is also reflected in the recorded number and amplitudes of the acoustic emission events during the test.
- The ARCTIC test was able to distinguish bitumen and mastic specimens regarding their resistance to thermal cracking, showing clearly that bitumen specimens deformed more and cracked at higher temperatures as compared to the mastic ones. The geometry of the specimens and the cooling rate chosen in this study, allowed to produce fracture in all the tests. However, additional testing is required in order to establish the test for a wider range of materials.

- Practical advantages of the proposed method are: Low-cost equipment with minimal instrumentation requirements and the possibility to conduct several tests simultaneously. The test is furthermore conducted on a notch-free specimen, which is more representative for the field conditions and removes the artefacts associated with the notch shape. In the ARCTIC test, the cracking temperature can be determined regardless of the type of crack and its location.
- With FE analysis it was shown that a considerable temperature gradient is induced in the specimen during the test, with the outer surface of the specimens being significantly colder than the boundary between the specimen and the invar core. As the measurement system used does not capture the location of fracture initiation, this temperature gradient introduces a certain uncertainty in the determination of the cracking temperature.
- According to the FE results, the maximum principal stress induced in the specimen during the ARCTIC test is higher at the boundary between the specimen and the invar core and is oriented in the circumferential direction. Most of the cracks are thus likely to start at this boundary and propagate in the radial direction, which is qualitatively consistent with the observed crack pattern.
- High cooling rates increase the temperature gradient of the specimen, whereas low cooling rates increase the degree of relaxation in the specimen and, accordingly, decrease the tensile stresses induced in the material. Hence, the cooling rate for testing should be chosen by optimizing these two effects, thus ensuring that sufficiently high tensile stresses are induced while the temperature gradient is kept as low as possible.

In view of the above results, this test method can be considered as a promising approach for evaluating the cracking susceptibility of bituminous binders, mastic and possibly also bitumen-aggregate composites with coarser aggregates such as mortar and, after some possible modifications, also for asphalt mixtures. The evaluation of the test feasibility for characterization of coarser binder-aggregate composites will be done as a part of future studies. In addition, the equipment used for the measurement of acoustic

emissions in this study, is very simplistic. The accuracy of the analysis may be improved considerably if more advanced instrumentation and analysis methods are used. This possibility will also be evaluated in the future.

Declarations

References

1. Kim J, Roque R, Birgisson B (2008) Integration of thermal fracture in the HMA fracture model. J Asph Paving Technol 77:631–661

2. Arabani M, Shabani A (2019) Evaluation of the ceramic fiber modified asphalt binder. Constr Build Mater 205:377–386. https://doi.org/10.1016/j.conbuildmat.2019.02.037

3. Zhang H, Xu G, Chen X, Wang R, Shen K (2019) Effect of long-term laboratory aging on rheological properties and cracking resistance of polymer-modified asphalt binders at intermediate and low temperature range. Constr Build Mater 226:767–777

4. Lu X, Uhlback P, Soenen H (2017) Investigation of bitumen low temperature properties using a dynamic shear rheometer with 4 mm parallel plates. Int J Pavement Res Technol 10(1):15–22

5. Kommidi SR, Kim Y-R (2021) Dynamic shear rheometer testing and mechanistic conversion to predict bending beam rheometer low temperature behavior of bituminous binder. Constr Build Mater 267:120563

6. Sebaaly PE, Lake A, Epps JA (2001) Evaluation of low temperature properties of HMA mixtures

7. Wu S (2017) Evaluate thermal cracking resistance of asphalt binder using 4-mm dynamic shear rheometer monotonic test. Pet Sci Technol 35(7):732–737

8. Zaumanis M, Valters A (2020) Comparison of two low-temperature cracking tests for use in performance-based asphalt mixture design. Int J Pavement Eng 21(12):1461–1469

9. Walubita LF, Fuentes L, Tanvir H, Chunduri HR, Dessouky S (2021) Correlating the asphalt-binder BBR test data to the HMA (ML-OT) fracture properties. J Mater Civ Eng 33(9):04021230

10. Bueno M, Hugener M, Partl MN (2014) Low temperature characterization of bituminous binders with a new cyclic shear cooling (CSC) failure test. Constr Build Mater 58:16–24

11. Bueno M, Hugener M, Partl M (2015) Fracture toughness evaluation of bituminous binders at low temperatures. Mater Struct 48(9):3049–3058

12. CEN/TS_15963 (2014) Determination of the fracture toughness temperature by a three point bending test on a notched specimen. European Committee for Standardization CEN, Brussels, Belgium

13. Behnia B, Buttlar WG, Reis H (2017) Nondestructive acoustic emission test to evaluate thermal damage in asphalt concrete materials. J Test Eval 46(1):118–126

14. Kim S-S (2005) Direct measurement of asphalt binder thermal cracking. J Mater Civ Eng 17(6):632–639

15. Hasan MRM, You Z (2019) Comparative study of ethanol foamed asphalt binders and mixtures prepared via manual injection and laboratory foaming device. J Traffic Transp Eng (English Edition) 6(4):383–395

16. Jin D, Ge D, Chen S, Che T, Liu H, Malburg L et al (2021) Cold in-place recycling asphalt mixtures: laboratory performance and preliminary me design analysis. Materials 14(8):2036

17. Liu J, Zhao S, Li L, Li P, Saboundjian S (2017) Low temperature cracking analysis of asphalt binders and mixtures. Cold Reg Sci Technol 141:78–85

18. Zhang R, You Z, Wang H, Ye M, Yap YK, Si C (2019) The impact of bio-oil as rejuvenator for aged asphalt binder. Constr Build Mater 196:134–143

19. Mogawer WS, Austerman AJ, Kim S-S (2013) Effect of binder type, mastic, and aggregate type on the low-temperature characteristics of modified hot mix asphalt. J Test Eval 41(6):914–923

20. Elwardany M, Planche J-P, King G (2020) Universal and practical approach to evaluate asphalt binder resistance to thermally-induced surface damage. Constr Build Mater 255:119331

21. Kim S-S, Wysong ZD, Kovach J (1962) Low-temperature thermal cracking of asphalt binder by asphalt binder cracking device. Transp Res Rec 1:28–35

22. Bahia HU, Faheem A, Hintz C, Al-Qadi I, Reinke G, Dukatz E (2010) NCHRP 9-45 Project "Test Methods and Specification Criteria for Mineral Filler Used in HMA". University of Wisconsin-Madison

23. Elseifi MA, Dessouky SH, Al-Qadi IL (1958) Yang S-H (2006) Viscoelastic model to describe mechanical response of bituminous sealants at low temperature. Transp Res Rec 1:82–89

24. Wang D, Wang L, Zhou G (2012) Fatigue of asphalt binder, mastic and mixture at low temperature. Front Struct Civ Eng 6(2):166–175

25. Hou Y, Wang L, Yue P, Pauli T, Sun W (2014) Modeling mode I cracking failure in asphalt binder by using nonconserved phase-field model. J Mater Civ Eng 26(4):684–691

26. Jahanbakhsh H, Karimi MM, Nejad FM, Jahangiri B (2016) Viscoelastic-based approach to evaluate low temperature performance of asphalt binders. Constr Build Mater 128:384–398

27. Bekele A, Balieu R, Jelagin D, Ryden N, Gudmarsson A (2021) Micro-mechanical modelling of low temperature-induced micro-damage initiation in asphalt concrete based on cohesive zone model. Constr Build Mater 286:122971

28. Zeng M, Shields DH (1999) Nonlinear thermal expansion and contraction of asphalt concrete. Can J Civ Eng 26(1):26–34

29. EN_12591 (2009) Bitumen and Bituminous Binders—Specifications for Paving Grade Bitumens. Committee for Standardization CEN, Brussels, Belgium

30. Engineering ToolBox (2003) Convective heat transfer. https://www.engineeringtoolbox.com/convective-heat-transfer-d_430.html. Accessed 27 Feb 2023

31. Lindberg WR, Thomas RR, Christensen RJ (1985) Measurements of specific heat, thermal conductivity and thermal diffusivity of Utah tar sands. Fuel 64(1):80–85

32. Gray MR (2019) Fundamentals of partial upgrading of bitumen. Energy Fuels 33(8):6843–6856

33. Refaa Z, Kakar MR, Stamatiou A, Worlitschek J, Partl MN, Bueno M (2018) Numerical study on the effect of phase change materials on heat transfer in asphalt concrete. Int J Therm Sci 133:140–150

34. Luo L, Liu P, Oeser M (2022) A molecular dynamics simulation study on enhancement of thermal conductivity of bitumen by introduction of carbon nanotubes. Constr Build Mater 353:129166

35. Zhou X, Wang S, Zhou C (2012) Thermal conduction and insulation modification in asphalt-based composites. J Mater Sci Technol 28(3):285–288

36. Park S, Schapery R (1999) Methods of interconversion between linear viscoelastic material functions. Part I—A numerical method based on Prony series. Int J Solids Struct 36(11):1653–1175

37. Mihora D, Friedman K, Hutchinson J (2012) Friction between steel and asphalt without gouging under representative rollover impact pressures. In: ASME international mechanical engineering congress and exposition, vol 45271, pp 213–217

38. Sundström B (2010) Handbook of solid mechanics. Department of Solid Mechanics, KTH

39. Rochlani M, Falla GC, Leischner S, Wellner F (2021) Towards a unified performance based characterisation of bitumen and mastic using the DSR. Road Mater Pavement Des 22:S365–S382

40. Rochlani M, Leischner S, Falla GC, Wang D, Caro S, Wellner F (2019) Influence of filler properties on the rheological, cryogenic, fatigue and rutting performance of mastics. Constr Build Mater 227:116974